Simulation of Radar Mountain Returns Using a Digitized Terrain Model

GUY DELRIEU AND JEAN DOMINIQUE CREUTIN

Laboratoire d'étude des Transferts en Hydrologie et Environnement (LTHE), Grenoble, France

HERVÉ ANDRIEU

Laboratoire Central des Ponts et Chaussées (LCPC), Bouguenais, France

(Manuscript received 6 October 1994, in final form 27 March 1995)

ABSTRACT

The aim of the present study is to characterize mountain returns measured with a ground-based weather radar operating in a mountainous region. A computation code based on the use of a digitized terrain model is developed for calculating the areas illuminated by the radar beam. Partial and total screening effects are accounted for in the calculation. The angular and range weighting functions of the radar measurement are modeled using Gaussian approximations to give the so-called weighted illuminated areas for various sizes of the radar resolution volume. Radar measurements are compared to the computed illuminated areas in order to determine the average backscattering coefficient of partly grass-covered, partly forested mountains: 87% of the measured time-averaged mountain return variance is explained by the computed values when the 15-dB resolution volume is considered. Additional geometrical information, provided by the calculated angles of incidence, is accounted for to yield a linear $\sigma^0_{(dB)}(\alpha)$ model relevant for the so-called near-grazing region since most of the angles of incidence are in the 70°–90° range. Here 92% of the measurement variance is explained when the $\sigma^0_{(dB)}(\alpha)$ model is used.

1. Introduction

From a meteorological point of view, mountainous relief plays an important role in generating or intensifying precipitation. Furthermore, from a hydrological point of view, it leads to reduced response times and increased streamflow volumes over small and potentially dangerous watersheds of mountainous areas. In this context, weather radar is a very useful device for estimating and forecasting rainfall compared to conventional rain gauge networks. However, its use comes up against major difficulties due to the interception of electromagnetic waves by the relief. Optimization of the radar location with respect to the areas of interest certainly minimizes ground clutter and screening effects. A volumetric scanning protocol is also compulsory to cancel residual ground clutter, to infer the vertical structure of atmospheric reflectivities, and to extend the spatial coverage of the radar measurement (Joss and Waldvogel 1990; Andrieu and Creutin 1995; Andrieu et al. 1995).

However, besides the obvious need for eliminating ground detection effects, a precise characterization of mountain returns can be interesting for various applications. First, mountains could be used as passive targets for continuous testing of radar calibration stability. Second, methods for improving rainfall estimation over ground-cluttered areas could be derived. Finally, when attenuating wavelengths are considered, mountain returns may be used for estimating path-integrated attenuation due to rainfall between the radar and the mountain. The interest of such additional information for correcting attenuated reflectivity profiles (surface reference technique) is now well established for a spaceborne radar configuration (e.g., Meneghini et al. 1983; Meneghini and Kozu 1990; Marzoug and Amayenc 1991, 1994).

The present work is a numerical approach to this characterization. A procedure for calculating areas illuminated by the radar beam using a digitized terrain model (DTM) is proposed. The angular and range weighting functions of the radar measurement, as well as partial or total screening effects, are accounted for in the establishment of the radar equation for ground targets. At the same time, X-band radar measurements realized in Grenoble, France, enable computation of time-averaged mountain returns during nonrainy conditions. These data, compared to the calculated illuminated areas, lead to a model for the mean backscattering coefficient of partly grass-covered and partly forested mountains.

Note that previous work has been done concerning the attractive idea of using DTMs for radar siting in mountainous areas: in France, we can mention a pi-

Corresponding author address: Dr. Guy Delrieu, LTHE, [UJF, INPG, CNRS (URA 1512)], BP 53 38041 Grenoble, Cedex 9, France.

oneer work by Roux et al. (1989) that was a quite successful attempt to simulate ground detections in the context of the Cévennes 1986–88 Hydrometeorological Experiment (Andrieu et al. 1989). The resulting code has been later improved by Météo France; it is currently used for choosing the sites of the new radars to be installed in the uncovered mountainous areas of the South of France (ARAMIS network).

2. Theory

a. Radar equation for a ground target

In an analogous way to the weather radar equation (Doviak and Zrnić 1992), the radar equation for a ground target may be written as follows:

$$\bar{P}(r_0, \theta_0, \phi_0) = \frac{P_t \lambda^2}{(4\pi)^3} \int\int_S \frac{G_t^2(\theta_b, \phi_b)|W(r_b)|^2}{r^4} \times \sigma^0(r, \theta, \phi) L^2(r, \theta, \phi) dS. \quad (1)$$

Here (r_0, θ_0, ϕ_0) are the spherical coordinates of a given radar cell center, dS represents an elementary illuminated area centered at (r, θ, ϕ), and (r_b, θ_b, ϕ_b) are the spherical coordinates taken with respect to the radar cell center; that is, $r_b = r - r_0$, $\theta_b = \theta - \theta_0$, $\phi_b = \phi - \phi_0$. As dry weather conditions are considered, we assume that the two-way attenuation factor $L^2(r, \theta, \phi)$ is equal to 1 (i.e., the attenuation by atmospheric gases is neglected). Term $\sigma^0(r, \theta, \phi)$ is the backscattering coefficient (or backscattering cross section per unit area) of the elementary illuminated area dS. Besides the geometric and electromagnetic properties of the target, the average backscattered power $\bar{P}(r_0, \theta_0, \phi_0)$ at the output of the radar receiver depends on (i) the working wavelength λ, (ii) the transmitted power P_t, and (iii) the so-called angular and range weighting functions $G_t^2(\theta_b, \phi_b)$ and $|W(r_b)|^2$, accounting for the characteristics of the antenna and the receiver, respectively. Note that the validity of (1) lies on the assumption of a phase independence of the scattering elements dS so that their elementary powers may be added (Skolnik 1990, chapter 12).

b. Weighting functions and resolution volume

The angular weighting function $G_t^2(\theta_b, \phi_b)$ can be defined as the product of the square of the antenna power gain G_0 along the beam axis and the square of the normalized power gain pattern $f^2(\theta_b, \phi_b)$:

$$G_t^2(\theta_b, \phi_b) = G_0^2 f^4(\theta_b, \phi_b). \quad (2)$$

If the radar antenna is a paraboloid of revolution, (2) simplifies to

$$G_t^2(\psi_b) = G_0^2 f^4(\psi_b), \quad (3)$$

where ψ_b is the angular distance from the beam axis. A coarse approximation of $G_t^2(\psi_b)$ may consist of assuming that the gain is constant across the 3-dB beamwidth ψ_3 and zero elsewhere. A more satisfactory solution lies in the use of a Gaussian approximation for the normalized power gain pattern (Probert-Jones 1962)

$$G_t^2(\psi_b) = G_0^2 \exp\left(-\frac{2\psi_b^2}{\gamma^2}\right), \quad (4)$$

with

$$\gamma^2 = \frac{\psi_3^2}{4 \ln 2}.$$

Of course, this approximation is valid only for part of the main lobe, and more complex fittings involving Bessel functions of second order (Doviak and Zrnić 1992) should be used if the sidelobes are to be correctly defined.

In a quite analogous way, the range weighting function $|W(r_b)|^2$ is used to weight the contribution of a scatterer located at range r to the power sampled at range r_0. A standard approximation is to assume that for a rectangular transmitted pulse of duration τ, only scatterers within a range $c\tau/2$ (where c is the speed of light) centered at r_0 contribute and receive an equal weight of 1; that is,

$$|W(r_b)|^2 = \begin{cases} 1, & |r_b| \leq c\tau/4 \\ 0, & \text{elsewhere.} \end{cases} \quad (5)$$

Doviak and Zrnić (1992) proposed an alternative approach for modeling the range weighting function based on the concept of matched filtering. They showed that due to the finite bandwidth of the receiver, a better approximation of $|W(r_b)|^2$ is given by

$$|W(r_b)|^2 = \left\{\frac{1}{2}[\text{erf}(x + b) - \text{erf}(x - b)]\right\}^2 \quad (6)$$

for a rectangular transmitted pulse and if a Gaussian frequency transfer function of the receiver is assumed. In (6), erf represents the error function:

$$\text{erf}(y) = \frac{2}{\pi^{1/2}} \int_0^y \exp(-t^2) dt, \quad (7)$$

and $a = \pi[2(\ln 2)^{1/2}]^{-1}$, $b = B_6 \tau a/2$, $x = 2aB_6 r_b/c$, where B_6 is the 6-dB bandwidth of the receiver.

When (4) and (6) are used to model the angular and range weighting functions, the resolution volume contributing to the backscattered power sampled at a given point (r_0, θ_0, ϕ_0) is a priori infinite. By convention, we will define the m-dB resolution volume V_m to be the volume circumscribed by the $2m$-dB contour of $G_t^2(\psi_b)|W(r_b)|^2$. The angle and range extents corresponding to this cutoff level will be denoted ψ_m and r_m, respectively. The volume V_m is then defined in three-dimensional space $\mathbf{R}^3$ as

$$V_m = \left\{M(r, \theta, \phi) \in \mathbf{R}^3, |r_b| \leq \frac{r_m}{2}, \psi_b \leq \frac{\psi_m}{2}\right\}. \quad (8)$$

From a geometrical point of view, V_m is the intersection of a circular cone with a ψ_m vertex angle and a spherical shell of outer radius $r_0 + r_m/2$ and inner radius $r_0 - r_m/2$.

c. Illuminated area

From the previous considerations and making the further assumption that the range extent of the resolution volume is small compared to r_0, (1) may be rewritten as follows:

$$\bar{P}(r_0, \theta_0, \phi_0) = C_S \frac{\Sigma^0}{r_0^4}, \tag{9}$$

where C_S is the radar constant relevant for a ground target

$$C_S = \frac{P_t G_0^2 \lambda^2}{(4\pi)^3}$$

and

$$\Sigma^0 = \int\int_S f^4(\psi_b) |W(r_b)|^2 \sigma^0(r, \theta, \phi) dS. \tag{10}$$

Let us consider a new variable Σ, the so-called weighted illuminated area, depending only on the geometric characteristics of the ground target and the radar beam:

$$\Sigma = \int\int_S f^4(\psi_b) |W(r_b)|^2 dS. \tag{11}$$

An estimation Σ_m of Σ (the subscript m refers to the size of the resolution volume) can be obtained using a DTM of the area of interest according to the following procedure. Let us consider an X, Y, Z rectangular coordinate system centered at O, the radar location. Figure 1 presents a schematic illustration of the vertical and horizontal projections of V_m. The DTM consists of a series of (X, Y, Z) triplets giving the altitude of ground for a regular grid with horizontal resolution $(\Delta X, \Delta Y)$. Hence, the ground surface is described by small portions of planes defined by three adjacent grid points. First, all the DTM grid points belonging to the (X, Y) projected area of V_m are selected. To each grid-point A, we can associate only two distinct triangles ABC and $AB'C'$ as shown in Fig. 1b. The weighted illumination area Σ_m will then be calculated as the discrete summation of the weighted illuminated areas of the N_t triangles thus defined:

$$\Sigma_m = \sum_{i=1}^{N_t} \Sigma_m(i). \tag{12}$$

Let us now consider the calculation of $\Sigma_m(i)$: the ith triangle defines a plane P_i in $\mathbf{R}^3$. The angle of incidence α_i of the electromagnetic waves on P_i is given by

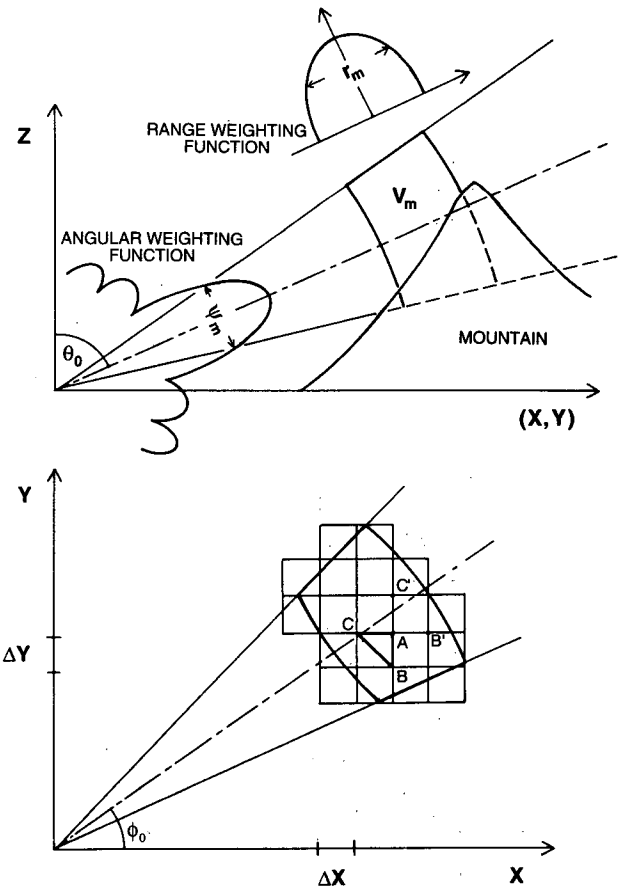

FIG. 1. (a) Vertical and (b) horizontal projections of the m-dB radar resolution volume in the (O, X, Y, Z) Cartesian coordinate system linked to the DTM.

$$\cos\alpha_i = -\mathbf{n} \cdot \mathbf{r}_0, \tag{13}$$

where $\mathbf{n}$ and $\mathbf{r}_0$ are the unit vectors normal to P_i and along the radar beam axis, respectively, oriented toward positive Z values (Fig. 2). Plane P_i is illuminated by the radar beam if $\alpha_i \leq \pi/2$. In such a case, the intersection of the circular cone and plane P_i is an ellipse if $\alpha_i \leq \pi/2 - \psi_m/2$ and an hyperbola if $\pi/2 - \psi_m/2 \leq \alpha_i \leq \pi/2$ (Florent et al. 1991). Due to the small values of ψ_m, we will consider only the case of an ellipse intersection in the following. Furthermore, the intersection of the spherical shell and plane P_i is a circular shell if $r_0 - r_m/2$ is greater than the distance between O and O', where O' is the projection of O on P_i. At this point, it is convenient to consider a new x, y, z rectangular coordinate system associated to plane P_i in order to obtain a simple parameterization of the ellipse and the circular shell. An integration scheme can then be applied to obtain $\Sigma_m(i)$, the limits of integration being given by the triangle, the ellipse, and the circular shell equations. It is worth noting that the integration procedure is complicated by two factors: first, the calculation of the weights $f^4(\psi_b)$ and $|W(r_b)|^2$

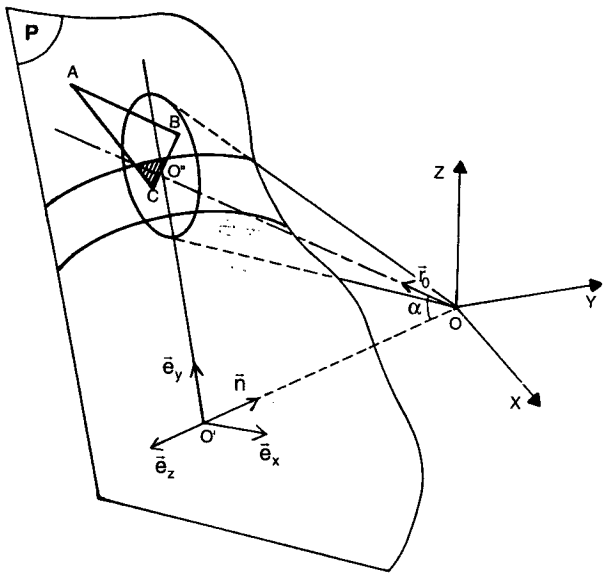

FIG. 2. Side view of the intersection of the radar resolution volume and an elemental planar surface generated by three adjacent DTM grid points.

imposes a conversion of the (x, y, z) coordinates back to the (r_b, θ_b, ϕ_b) coordinates; second, an additional integration constraint is required to account for possible partial or total screening effects due to the interception of the radar beam prior the range cell of interest. Details concerning this integration procedure are given in the appendix.

d. Backscattering coefficient

The backscattering coefficient of ground depends both on the nature of the surface (roughness, vegetation cover, moisture content, etc.) and on the radar parameters (wavelength, angle of incidence, polarization of the waves, etc.). Moore (Skolnik 1990, chapter 12) reviews various models for backscattering coefficients obtained from either satellite radiometer or with mast-mounted microwave active spectrometer measurements. For instance, a so-called linear model was fitted to average backscattering coefficients versus the angle of incidence:

$$\bar{\sigma}^0 = A_0 \exp\left(-\frac{\alpha}{\alpha_0}\right). \tag{14}$$

This model is said to be linear since its logarithmic transform yields

$$\bar{\sigma}^0_{(\mathrm{dB})} = a_0 + b_0\alpha, \tag{15}$$

with $a_0 = 10 \log A_0$ and $b_0 = -4.343/\alpha_0$. The parameters a_0 and b_0 are wavelength and polarization dependent (see Table 12-2 in Skolnik 1990). Their validity is also restricted to a given range of angles of incidence. Basically, according to Moore, three angular "regimes" can be distinguished: the near-vertical regime corresponding to angles of incidence ranging from 0° to 15°, the plateau region corresponding to angles of incidence ranging from 15° to about 70°, and the near-grazing regime for angles of incidence greater than 70°.

In the measurement context considered in the present study, we can infer such a linear model through the comparison of measured values of Σ^0 and values of Σ calculated according to the procedure described in section 2c. On one hand, N observations of Σ^0 can be obtained for all radar cells giving mountain returns over the measurement area. If n is a space index ($n = 1, N$) for the radar measurement made at point (r_0, θ_0, ϕ_0), (9) gives

$$\Sigma^0(n) = \frac{\bar{P}(r_0, \theta_0, \phi_0) r_0^4}{C_S}. \tag{16}$$

On the other hand, to each triangle i contributing to the estimation of the nth illuminated area, [$i = 1$, $N_t(n)$] can be associated the values of $\Sigma_m(i, n)$ and $\alpha_i(n)$. Equation (12) yields

$$\Sigma_m(n) = \sum_{i=1}^{N_t(n)} \Sigma_m(i, n). \tag{17}$$

The statistical distribution of the calculated angles of incidence $\alpha_i(n)$ gives the range of angles of interest [$\alpha_{\min}, \alpha_{\max}$], which can be divided into N_α classes using a $\Delta\alpha$ step. Rearranging the Σ_m values according to the N_α classes of angles enables (17) to be written as follows:

$$\Sigma_m(n) = \sum_{j=1}^{N_\alpha} \Sigma_m(\alpha_j, n), \tag{18}$$

where α_j is the central value of the jth class of angles of incidence. Equations (16) and (18) can be combined as

$$\Sigma^0(n) \equiv \sum_{j=1}^{N_\alpha} \sigma^0(\alpha_j)\Sigma_m(\alpha_j, n), \tag{19}$$

where the [$\sigma^0(\alpha_j)$, $j = 1, N_\alpha$] values are coefficients that can be estimated over the N available observations using a multiple regression scheme.

3. Case study

a. Experimental context and dataset

Grenoble is located in the French Alps at the confluence of the Isère and Drac Rivers. The topography of the city is very flat with a mean altitude of 210 m above sea level. The city is surrounded by three mountain chains (Belledonne, Chartreuse, and Vercors) with maximum altitudes ranging from 2000 up to 3000 m (Fig. 3). During the last few years, various hydrometeorological experiments were conducted by the LTHE for developing and testing a prototype X-band weather radar devoted to rainfall monitoring at the time and

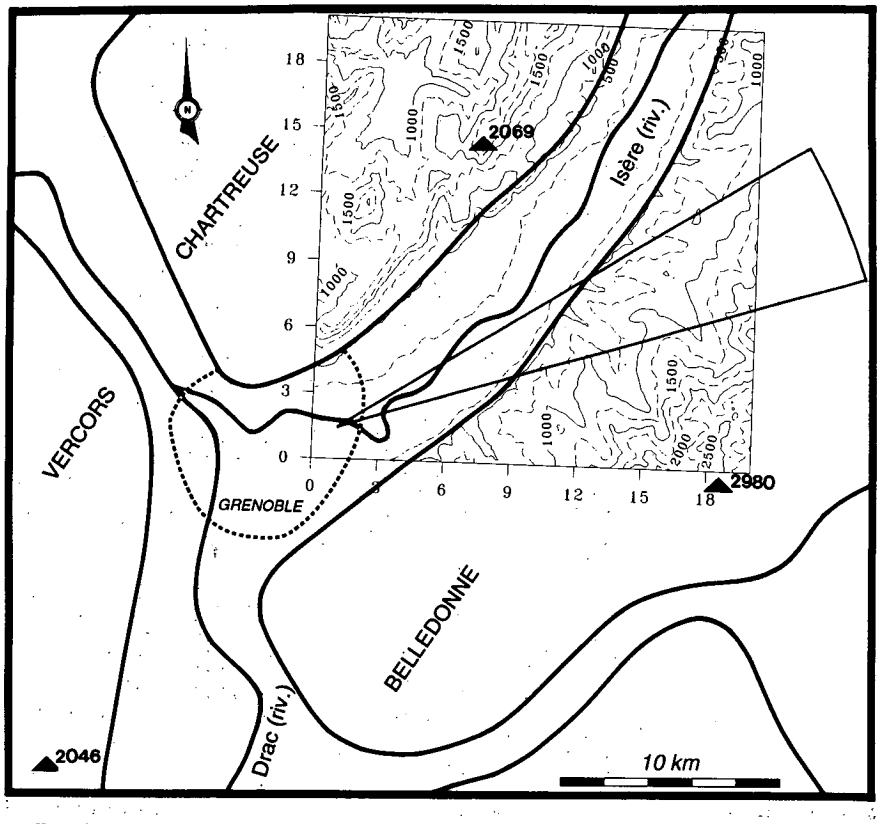

FIG. 3. Presentation of the study area: the available DTM information (250-m isolines), the radar location, and the measurement sector are situated on a schematic view of the Grenoble area.

space scales useful for urban hydrology (Delrieu and Creutin 1991). The main features of the system are listed in Table 1. During spring 1994, a specific experiment was conducted for studying the behavior of mountain returns during nonrainy conditions. For convenience, the radar was located on the roof of the laboratory (Grenoble campus) down in the valley. A digitized terrain model (provided by the French Institut Géographique National) with a resolution of $\Delta X = \Delta Y = 100$ m is available for part of the area of interest (Fig. 3). The measurement effort was concentrated on a reduced azimuthal sector (60°–75°) for characterizing radar returns due to the partly forested and partly grass-covered Balcons de Belledonne Mountains. A volumetric scanning protocol at two elevations (2° and 3.5°) was repeated every 3 min. Special care was paid to the selection of the azimuths and elevations in order to avoid receiver saturation effects. During the measurement period, the weather was good and the mountain surfaces were considered relatively dry with no snow cover. Figure 4 gives an illustration of the temporal evolution of mountain returns during the measurement period: the space-averaged Σ^0 value is displayed as a function of time. It can be noted that the mountain returns are relatively constant within each measurement period and from one measurement period to another. This fact tends to prove the good overall stability of the radar calibration and explains the calculation of Σ^0 temporal averages for the present $\sigma^0(\alpha)$ model inference. The electronic calibration [in-

TABLE 1. The X-band radar parameters.

Transmitter–receiver	
Peak power	25 kW
Frequency	9.375 GHz
PRF	500 Hz
Pulse width	2 μs
MDS	−109 dBm
Receiver 6-dB bandwidth	1 MHz
Receiver conversion slope	0.3 dB per count
Antenna	
Diameter	1.2 m
Beamwidth at half power	1.8°
Power gain	38.8 dB
Polarization	Horizontal
Data features	
Maximum range used	25 km
Radial resolution	250 m
Incremental azimuth	0.5°
Number of power levels	256

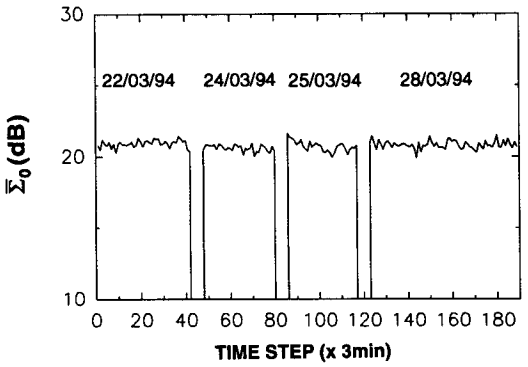

FIG. 4. Temporal evolution of the space-averaged mountain returns over the measurement area during four successive periods [22 March 1994 (126 min), 24 March 1994 (99 min), 25 March 1994 (96 min), and 28 March 1994 (201 min)] taken in similar weather conditions.

cluding standard alignments and measurements of some of the parameters involved in the radar equation (peak power, frequency, pulse width . . .), as well as a characterization of the receiver response using a signal generator] was performed with the help of the radar manufacturer. Complementary measurements concerning the antenna power gain pattern were also realized using a homemade receiver located at some distance of the radar. The absolute calibration, also checked using rain gauge data during various rainfall events, is estimated to be accurate to within ±1 dB.

b. *Comparison of measured Σ^0 and simulated Σ values*

1) PRELIMINARY TESTS AND ADJUSTMENTS

First, the computation code was tested using simulated DTMs in order to check the validity of the unweighted illuminated areas (S_m) and angles of incidence calculation. Special care was paid to the choice of the $(\Delta x, \Delta y)$ integration steps and to the mask grid resolution $[\Delta \tan(\theta_b), \Delta \tan(\psi_b)]$ (see the appendix) in relation to the range of distances and angles of incidence considered. To give an example, $\Delta x = \Delta y = 1$ m and $\Delta \tan(\theta_b) = \Delta \tan(\psi_b) = 1.1 \times 10^{-4}$ were found to provide a very good estimation (often much better than 1% for S_m) for a reasonable computing time.

Second, the angular and range weighting functions (Fig. 5) were calculated using (4) and (6) and the relevant parameters listed in Table 1. Note the good agreement of the Gaussian approximation of the angular weighting function with the measurements. Table 2 gives the corresponding angular and range extents ψ_m and r_m for the m-dB resolution volumes considered, that is, for $m = 3, 6, 9, 12$, and 15 dB. It is worth noting that the application of the range weighting function further complicates the computation code since (i) the radar measurements have a 250-m radial resolution and (ii) the procedure accounting for screening effects

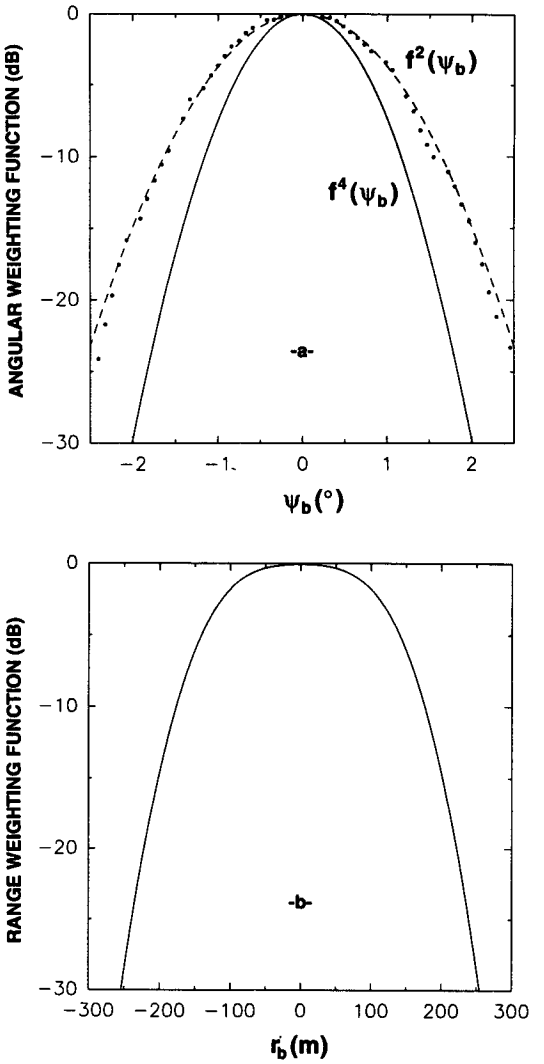

FIG. 5. Angular and range weighting functions: (a) measured antenna power gain pattern $f^2(\psi_b)$ (points) and its Gaussian approximation (dotted line) using $\psi_3 = 1.8°$, together with the resulting angular weighting function $f^4(\psi_b)$; (b) range weighting function $|W(r_b)|^2$ obtained with the measured pulse width ($\tau = 2$ μs) and 6-dB receiver bandwidth ($B_6 = 1$ MHz) values using Eq. (6).

requires the use of nonoverlapping radial cells. To solve this problem, the code was activated twice for a single calculation with 500-m radial cells: one time with radial

TABLE 2. Angular and range extents of the m-dB resolution volume.

m (dB)	ψ_m (°)	r_m (m)
3	1.80	300
6	2.54	375
9	3.10	429
12	3.60	472
15	4.00	509

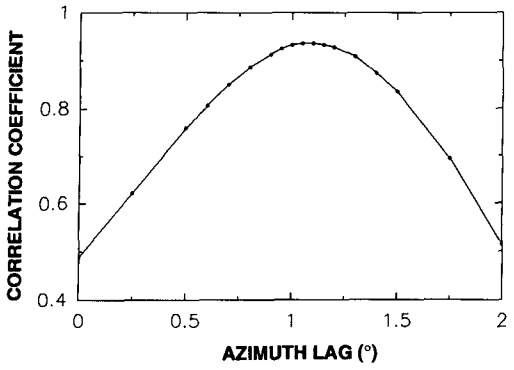

FIG. 6. Correlation coefficient of the measured Σ^0 values and calculated Σ_m values (m = 15 dB) as function of the azimuth lag introduced in the geometrical calculation: an azimuth pointing error of about 1° is visible and was verified by the means of a detailed point target azimuth analysis.

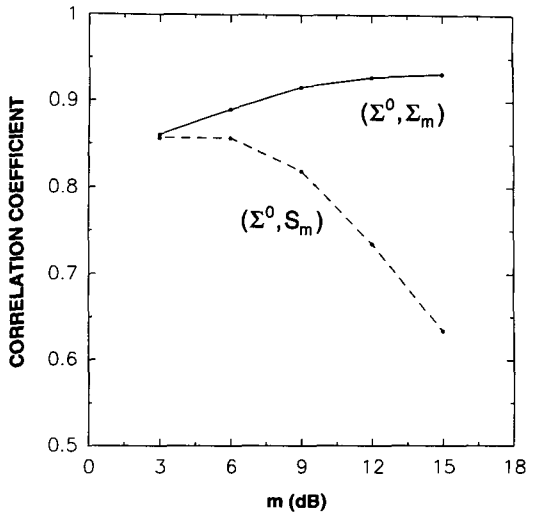

FIG. 7. Influence of the weighting functions and resolution volume size: the correlation coefficients of the measured Σ^0 values (i) versus the computed unweighted areas S_m (dotted line) and (ii) versus the computed weighted areas Σ_m (solid line) are displayed as functions of the m-dB radar resolution volume size.

cells centered on one over two radar bins and a second time with a shift of 250 m in order to produce Σ_m estimates for the remaining radar bins.

Finally, as the radar positioning may present some systematic error, the first comparisons of measured Σ^0 and calculated Σ_m values were utilized for the estimation of azimuth, zenith, and radial lags using as a criteria the correlation coefficient ρ of the (Σ^0, Σ_m) pairs. The most striking result is presented in Fig. 6 (note that the 15-dB resolution volume was considered in the Σ_m calculation): an azimuth error of about 1.0° is clearly identified, a moderately surprising result owing to the azimuth positioning technique initially used (adjustment using surrounding "broad" targets such as mountaintops). The amplitude and orientation of the lag was confirmed later by a detailed azimuth analysis based on a more ponctual target (radio tower). Hence, the proposed geometrical calculation is thought to offer as a by-product a solution for checking radar angular positioning with an accuracy comparable to the sun's positioning technique (±0.1°).

2) INFLUENCE OF THE WEIGHTING FUNCTIONS AND RESOLUTION VOLUME SIZE

Figure 7 presents the correlation coefficients obtained between the measured Σ^0 and (i) the calculated unweighted areas S_m and (ii) the calculated weighted areas Σ_m for various sizes of the resolution volume (m = 3, 6, 9, 12, 15 dB). Concerning the (Σ^0, S_m) comparison, it can be seen that ρ is stable for m = 3 and m = 6 and then rapidly decreases for higher-resolution volume sizes. Note that the 3-dB case (ρ = 0.857) corresponds to the simplest models for the angular and range weighting functions evoked in section 2b. Furthermore, the (Σ^0, Σ_m) correlation coefficient significantly increases from m = 3 dB (ρ = 0.861) to m = 12 dB (ρ = 0.930) and then becomes stable (ρ = 0.932 for m = 15 dB). The interest of using more complex models for the angular and range weighting functions [such as the Gaussian approximations given by (4) and (6)] is therefore clearly established in the case of mountain returns observed with a ground-based radar. The "sill" value for $m \geq 12$ is certainly due to the fact that scattering surfaces outside the 12-dB volume receive almost negligible weights (less than 4.0×10^{-3}).

c. *Inference of the backscattering coefficient model*

The histogram of the angles of incidence calculated for each illuminated triangle contributing to the Σ_m estimations over the measurement area (N = 941) is presented in Fig. 8. It is worth noting that according to Moore's classification (see section 2d), the observed α range basically corresponds to the near-grazing region: the distribution is unimodal with a mean value of 77.0° and a standard deviation of 5.7°; the cumu-

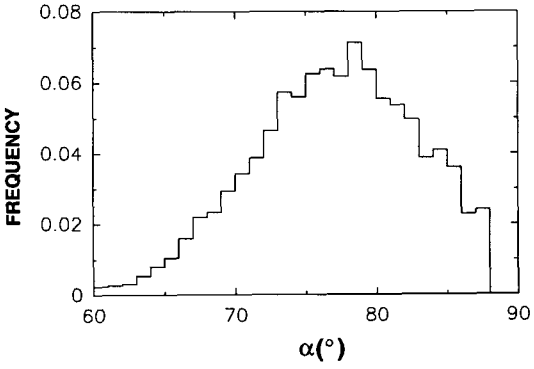

FIG. 8. Histogram of the calculated angles of incidence.

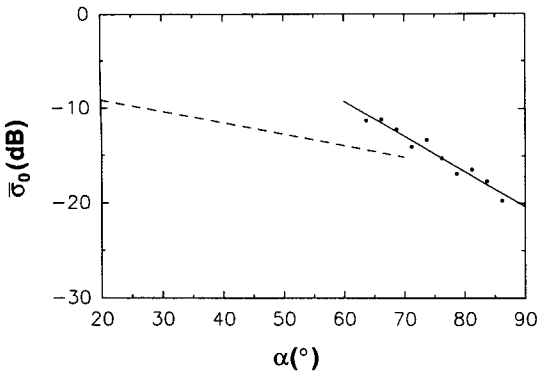

FIG. 9. Average backscattering coefficient as function of the angle of incidence: the points represent the $[\sigma^0(\alpha_j), j = 1, N_\alpha]$ coefficients given by a multiple regression analysis. The linear regression line fitted to these coefficients in order to obtain the $\bar{\sigma}^0_{(dB)}(\alpha)$ linear model parameters [Eq. (20)] is represented by the solid line. The dotted line gives the model proposed by Skolnik (1990).

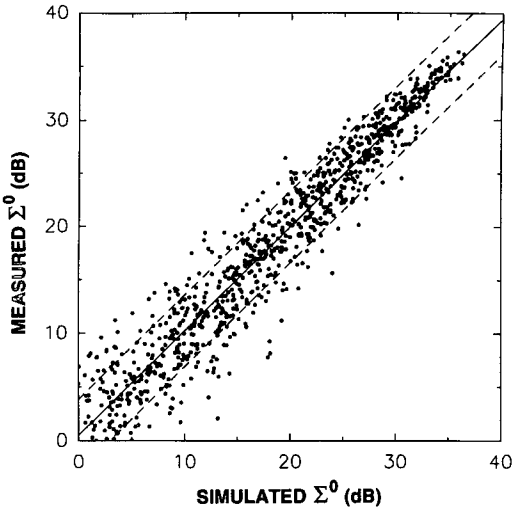

FIG. 10. Scattergraph of the computed and measured mountain returns, together with the corresponding regression line and the 80% confidence intervals. Note that the computed Σ^0 values are obtained with the 15-dB resolution volume and the $\sigma^0(\alpha)$ model given by Eq. (21).

lative frequency of the α values less than 60° is negligible, and the upper limit ($\pi/2 - \psi_m/2 = 88°$ for $m = 15$, see section 2c) introduces a minor truncation effect. The following α partition was chosen for the backscattering coefficient model inference according to the procedure described in section 2d:

$$N_\alpha = 10 \quad \Delta\alpha = 2.5° \quad \alpha_1 = 63.75°,$$

corresponding to an α range of [62.5°–87.5°]. The resulting $[\sigma^0(\alpha_j), j = 1, N_\alpha]$ coefficients, expressed in decibel values are displayed in Fig. 9. A regression line was fitted to these coefficients (with a correlation coefficient of −0.975) in order to estimate the (a_0, b_0) linear model parameters, yielding

$$\bar{\sigma}^0_{(dB)} = 12.93 - 0.37\alpha \tag{20}$$

or

$$\bar{\sigma}^0 = 19.61 \exp\left(-\frac{\alpha}{11.75}\right). \tag{21}$$

d. Consistency of the results

First, the $\bar{\sigma}^0(\alpha)$ model (21) was used to produce simulated values of Σ^0 according to the following equation:

$$\Sigma^0_m(n) = \sum_{i=1}^{N_i(n)} \bar{\sigma}^0(\alpha_i)\Sigma_m(i, n). \tag{22}$$

The calculated 15-dB weighted illuminated areas and the calculated angles of incidence as well were considered in this computation. The measured versus calculated Σ^0 values are plotted in Fig. 10 together with the corresponding regression line and the 80% confidence intervals. Although this comparison does not constitute a validation, it is useful for checking the overall consistency of the geometrical calculation procedure. It can be seen that the use of the $\bar{\sigma}^0(\alpha)$ model contributes a significant amount of information since the correlation coefficient is equal to 0.960 (i.e., 92% of explained variance), while the correlation coefficient of the (Σ^0, Σ_m) pairs is 0.932 (i.e., 87% of explained variance). Furthermore, the fact that the slope of the regression line is close to 1 tends to prove the overall quality of the shape parameters (such as the 3-dB beamwidth of the antenna, the 6-dB bandwidth of the receiver, the receiver conversion slope, etc.) used in the calculation procedure and the radar data processing. Indeed, a sensitivity study of these parameters has shown that improper estimation of their values may lead to significant biases in the measured and calculated Σ^0 correlations. As an illustration, Table 3 presents the slopes and correlation coefficients obtained when the 3-dB beamwidth of the antenna varies from 1.6° up to 2.0°.

Second, the $\bar{\sigma}^0(\alpha)$ model given by (20) and (21) can be compared to the models presented in Table 12-2 of Skolnik (1990) for the average backscattering

TABLE 3. Sensitivity of the measured and calculated Σ^0 values correlation to the 3-dB beamwidth of the antenna.

ψ_3 (°)	Correlation coefficient	Regression slope
1.6	0.950	0.84
1.7	0.957	0.91
1.8	0.960	0.97
1.9	0.960	1.05
2.0	0.958	1.12

coefficients of the summer Skylab (including a wide variety of land uses, such as desert, grassland, cropland, forest) and Kansas experiments (devoted to cropland measurements). The following equation was fitted to the data:

$$\bar{\sigma}^0_{(\mathrm{dB})}(f, \alpha) = a_1 + b_1\alpha + c_1 f + d_1 f\alpha, \quad (23)$$

where f is the frequency. For an angular range of 20°–70°, a frequency range of 6–17 GHz, and a horizontal polarization, the proposed values for the constants are $a_1 = -9.1$ dB, $b_1 = -0.12$ dB deg^{-1}, $c_1 = 0.25$ dB GHz^{-1} and $d_1 = 0$, yielding for $f = 9.375$ GHz:

$$\bar{\sigma}^0_{(\mathrm{dB})} = -6.76 - 0.12\alpha. \quad (24)$$

It can be noted (Fig. 9) that the models given by (20) and (24) are quite consistent owing to the different conditions of measurement: the average difference of the two curves in the 60°–90° angular range is about 1 dB. However, the mountain model presents a much higher slope (−0.37 instead of −0.12): this fact may be explained by the different behavior of the backscattering coefficient in the plateau and near-grazing regions. This last result has motivated an additional test for checking the sensitivity of the Σ^0 computation to the slope parameter of the $\bar{\sigma}^0_{(\mathrm{dB})}(\alpha)$ model: b_0 was allowed to vary in the [0, −1.0] range, while the corresponding intercept was calculated as $a_0 = \bar{\Sigma}^0 - \bar{\Sigma}_m - b_0\bar{\alpha}$, where $\bar{\Sigma}^0$, $\bar{\Sigma}_m$, and $\bar{\alpha}$ are the means of the measured Σ^0 values and the computed Σ_m and α values, respectively. It can be observed (Table 4) that the slope and the correlation coefficient of the measured and computed Σ^0 values increase from $b_0 = 0$ up to $b_0 = -0.2$, remain almost constant up to $b_0 = -0.5$, and then progressively decrease for higher slopes. Although the b_0 parameter influence is low in the [−0.2, −0.5] range, this result tends to confirm the significance of the $b_0 = -0.37$ estimation given by the multiple regression analysis.

Finally, a spatial display of the measured and calculated mountain returns over the measurement area is proposed in Fig. 11 for the two elevation angles considered. The overall agreement is good, especially for the strongest returns. The main differences can be depicted at the edge of cluttered areas and concern weak returns. This result is certainly due to both (i) the geometrical calculation uncertainty that is expected to increase when the illuminated area decreases and (ii) the expected higher variability of the weakest measured mountain returns. Note also that the coherence of the pictures does not seem to downgrade when the range increases, an indication of the good behavior of the partial screening procedure. This last result was confirmed by a correlation analysis of the Σ^0 values sorted into various range classes.

4. Conclusions

The present study was devoted to the characterization of time-averaged mountain returns measured with a ground-based X-band weather radar operating in a mountainous region. A computation code, based on the use of a digitized terrain model, was developed for calculating the areas illuminated by the radar beam. Partial and total screening effects were accounted for in the calculation. Furthermore, the angular and range weighting functions of the radar measurement were modeled using Gaussian approximations to give the so-called weighted illuminated areas for various sizes of the radar resolution volume.

TABLE 4. Sensitivity of the measured and calculated Σ^0 values correlation to the slope parameter of the backscattering coefficient model.

b_0	Correlation coefficient	Regression slope
0	0.932	0.92
−0.12	0.950	0.94
−0.20	0.958	0.96
−0.37	0.960	0.97
−0.50	0.955	0.95
−0.75	0.921	0.89
−1.00	0.870	0.80

It was shown that these geometrical estimates explain 87% of the radar measurement variance when the 15-dB resolution volume is considered. The explained variance is reduced to 73% for the unweighted illuminated areas of the 3-dB resolution volume, a result indicating that the simplest approximations of the range and angular weighting functions are unsatisfactory in the present context.

Then, the radar measurements and the simulated weighted areas were used to establish a model for the average backscattering coefficient $\bar{\sigma}^0$ of grass-covered and/or forested mountains. Additional geometrical information, provided by the calculated angles of incidence α, was accounted for to yield a linear $\bar{\sigma}^0_{(\mathrm{dB})}(\alpha)$ model consistent with the models proposed elsewhere in the literature. It is worth noting that this model is relevant for the so-called near-grazing region since most of the angles of incidence are in the 70°–90° range. A further gain was obtained with the use of the $\bar{\sigma}^0_{(\mathrm{dB})}(\alpha)$ model since the variance explained by the calculated mountain returns reaches 92% of the measurement variance. Furthermore, the slope of the regression between the calculated and measured values is close to 1, a result indicating the overall quality of the parameters used in the geometrical calculation and in the radar data processing.

Future work will be devoted to the characterization of the space and time variability of dry-weather mountain returns for various types of land uses (forest, grass, rocks, snow-covered surfaces, etc.). This information will serve as a base for studying the behavior of mountain returns in the presence of rain, the main objective being to assess the feasibility of using mountain returns for esti-

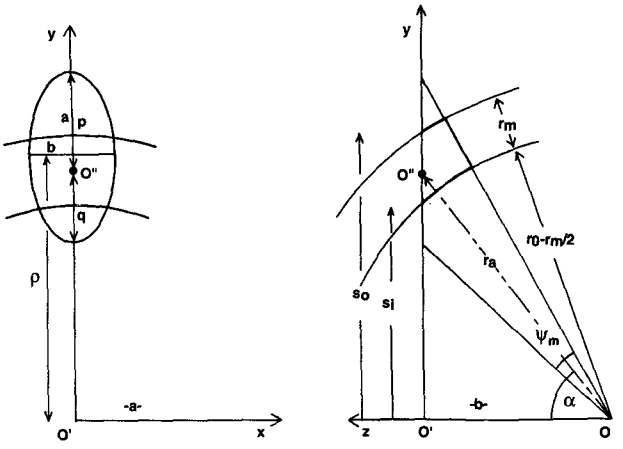

FIG. A1. Projections of the radar resolution volume (a) in the plane P generated by three adjacent DTM grid points and (b) in the plane normal to P defined by the triplet of points (O, O', O'').

of the spherical shell and plane P is a circular shell centered at O' (Fig. A1b).

It is convenient to consider a new x, y, z rectangular coordinate system, associated to plane P, defined as

$$\mathbf{e}_x = \mathbf{e}_y x \mathbf{e}_z$$

$$\mathbf{e}_y = \frac{\mathbf{r}_0 - \mathbf{e}_z \cos\alpha}{|\mathbf{r}_0 - \mathbf{e}_z \cos\alpha|}$$

$$\mathbf{e}_z = -\mathbf{n}, \tag{A1}$$

where $\mathbf{n}$ and $\mathbf{r}_0$ are the unit vectors normal to P and collinear to the radar beam axis, respectively, oriented toward positive Z values. Note that the y and x axis correspond to the main and the minor ellipse axes, respectively, and that the z axis is normal to P.

The parameterization of the ellipse and the circular shell can be obtained in the (O', x, y, z) coordinate system (Fig. A1).

The ellipse has for an equation

$$\frac{x^2}{a^2} + \frac{(y-\rho)^2}{b^2} = 1, \tag{A2}$$

with

$$a = \frac{1}{2}(p+q)$$

$$b = r_a \tan\left(\frac{\psi_m}{2}\right)\left[1 - \frac{(p-q)^2}{(p+q)^2}\right]^{-1/2}$$

$$\rho = r_a \sin\alpha + \frac{p-q}{2}$$

and

$$p = r_a \sin\left(\frac{\psi_m}{2}\right)\left[\cos\left(\alpha + \frac{\psi_m}{2}\right)\right]^{-1}$$

$$q = r_a \sin\left(\frac{\psi_m}{2}\right)\left[\cos\left(\alpha - \frac{\psi_m}{2}\right)\right]^{-1},$$

where r_a is the distance between the radar location (O) and the intercept (O'') of the radar beam axis with plane P.

The circular shell is limited by two circles centered at O' with equations

$$x^2 + y^2 = s_i^2$$

$$x^2 + y^2 = s_o^2, \tag{A3}$$

with

$$s_i = \left(r_0 - \frac{r_m}{2}\right)\sin\alpha$$

$$s_o = \left(r_0 + \frac{r_m}{2}\right)\sin\alpha.$$

Note that if r_0 and α are great enough, the circular shell can be approximated by a band limited by two lines parallel to the x axis with equations

$$y = s_i$$

$$y = s_o. \tag{A4}$$

Then the estimation of the weighted illuminated area can be performed by an integration scheme illustrated in Fig. A2. First the y range of integration is defined as

$$y_m = \max(y_m^E, y_m^S, y_m^T)$$

$$y_M = \min(y_M^E, y_M^S, y_M^T),$$

where the subscripts m and M refer to the minimum and maximum y values and the superscripts E, S, and T refer to the ellipse, the circular shell, and the triangle, respectively. If y_m is greater than y_M, the triangle is not illuminated. On the contrary, the $[y_m, y_M]$ interval is

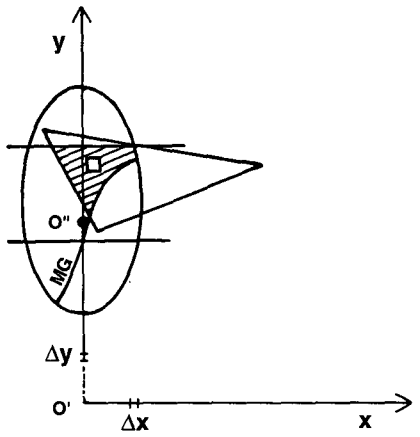

FIG. A2. Schematic illustration of the numerical integration procedure for estimating the illuminated area as the intersection of the ellipse, the circular shell (approximated by a linear band), the DTM triangle, and the so-called mask-grid constraint (MG line) due to the eventual interception of the radar beam by the relief at prior range cells.

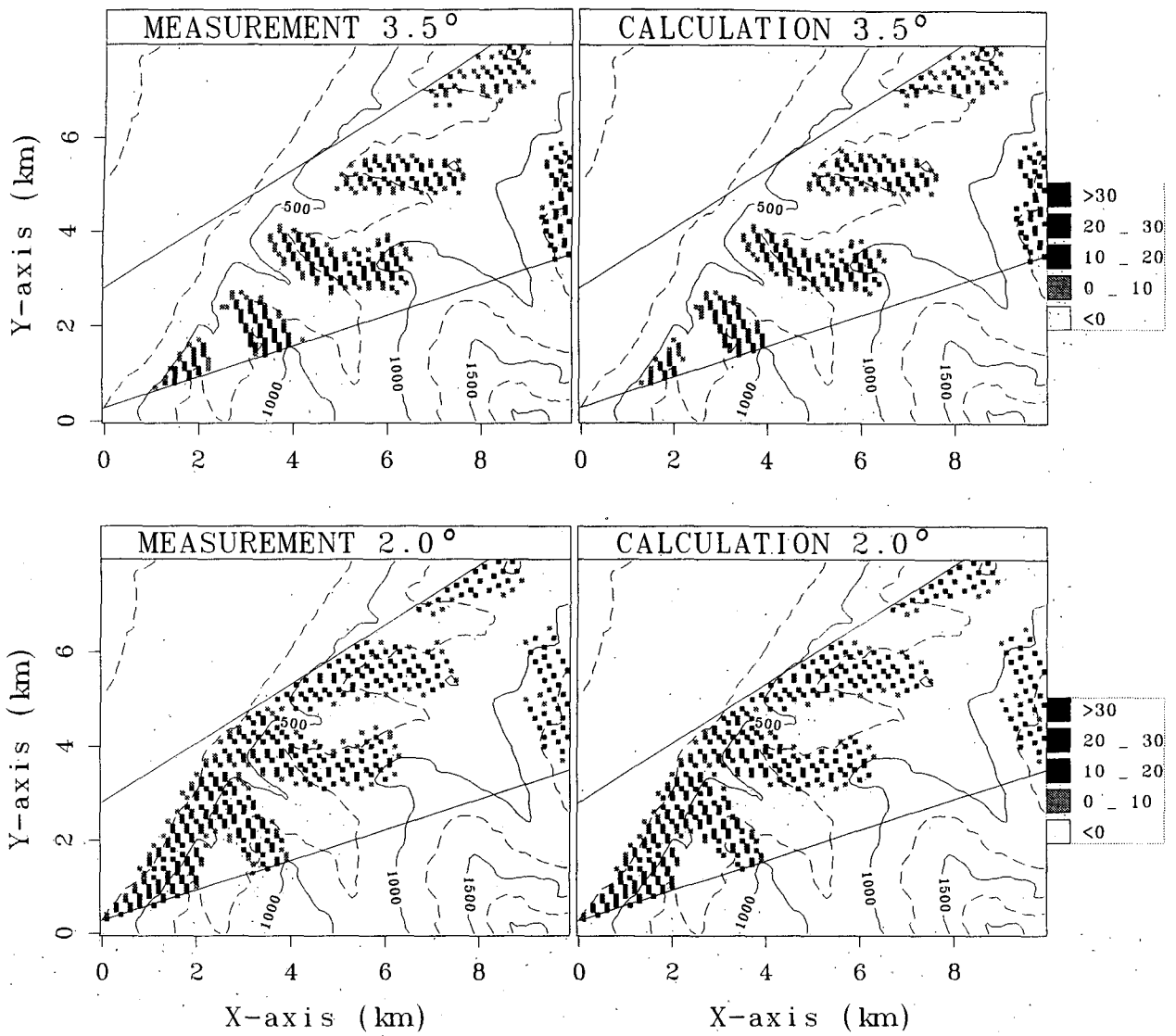

FIG. 11. Measured and calculated mountain returns for the two elevation angles considered (3.5° and 2.0°) in the radar measurement sector. Each polar Σ^0 value (expressed in decibels) is affected by the corresponding small Cartesian mesh (100 m × 100 m) in order to keep the underlying relief isolines visible.

mating path-integrated attenuation due to rainfall between the radar and the mountain target. This information is thought to be useful for correcting reflectivity profiles when attenuating wavelengths are used.

Acknowledgments. The contributions of Jochen Dreyer and Lise Lott Larson (Master of Physics students at the Joseph Fourier University in Grenoble, France) in the early development and testing of the computation code are greatly acknowledged. The present study was made under the Radar Hydrology Project funded by the Environment Framework Program of the European Community under Grant EV5V-CT92-01823.

APPENDIX

Calculation of the Intersection of the Radar Resolution Volume and an Elemental Planar Mountain Surface

Let us consider a plane P generated in $\mathbf{R}^3$ by a triplet of points (A, B, C). As noted in section 2b, the m-dB radar-resolution volume V_m is defined by the intersection of a circular cone with a ψ_m vertex angle and a spherical shell of outer radius $r_0 + r_m/2$ and inner radius $r_0 - r_m/2$. If the angle of incidence α [Eq. (13)] is less than or equal to $\pi/2 - \psi_m/2$, the intersection of the circular cone and plane P is an ellipse (Fig. A1a). Furthermore, if $r_0 - r_m/2$ is greater than the distance between the radar location and plane P, the intersection

discretized using a Δy step. For each y_k value [$y_k = y_m + \Delta y(k - 1/2)$], an x_k range of integration is defined as

$$x_m(y_k) = \max[x_m^E(y_k), x_m^T(y_k)]$$
$$x_M(y_k) = \min[x_M^E(y_k), x_M^T(y_k)],$$

where x_m^E, x_M^E, x_m^T, and x_M^T are the minimum and maximum $x(y_k)$ values for the ellipse and the triangle, respectively. The contribution of the kth y interval to the illuminated area is zero if $x_m(y_k) \geq x_M(y_k)$. On the contrary, the $[x_m(y_k), x_M(y_k)]$ range is discretized using a Δx step, thus leading to a series of elemental rectangular surfaces having a $\Delta x \Delta y$ size. These elemental surfaces are illuminated if there is no screening effect due to the interception of the radar beam prior the range cell of interest. To cope with this last problem, a so-called mask grid, defined in the plane normal to the beam axis with a [$\Delta \tan(\theta_b)$, $\Delta \tan(\phi_b)$] resolution, was used. First the spherical coordinates (r_b, θ_b, ϕ_b) of each elemental $\Delta x \Delta y$ surface center must be calculated. Then the mask grid meshes are progressively filled with the radar cell index of the first $\Delta x \Delta y$ surface falling into them. A $\Delta x \Delta y$ surface corresponding to a mask grid mesh already filled by a prior cell is considered as screened and, therefore, is not accounted for in the calculation of the weighted illuminated area. Furthermore, when all the mask grid meshes are filled, the radar beam is considered as totally screened and the Σ_m calculation is stopped for the current radar beam axis position. Note that the spherical coordinates (r_b, θ_b, ϕ_b) of each $\Delta x \Delta y$ surface center are also necessary to evaluate the angular and radial weights this surface will receive in the Σ_m calculation.

REFERENCES

Andrieu, H., and J. D. Creutin, 1995: Identification of vertical profiles of radar reflectivity using an inverse method. Part I: Formulation. *J. Appl. Meteor.*, **34,** 225–239.

——, G. Delrieu, and J. D. Creutin, 1995: Identification of vertical profiles of radar reflectivity using an inverse method. Part II: Sensitivity analysis and case study. *J. Appl. Meteor.*, **34,** 240–259.

——, J. D. Creutin, G. Delrieu, J. Léoussoff, and Y. Pointin, 1989: Radar data processing for hydrology in the Cévennes region. *Proc. of the IAHS Third International Assembly,* **189,** 105–115.

Delrieu, G., and J. D. Creutin, 1991: Weather radar and urban hydrology: Advantages and limitations of X-band weather systems. *Atmos. Res.*, **27,** 159–168.

Doviak, R. J., and D. S. Zrnić, 1992: *Doppler Radar and Weather Observations.* 2d ed. Academic Press Inc., 562 pp.

Florent, P., G. Lauton, and M. Lauton, 1981: *Calcul Vectoriel, Géométrie Analytique.* Collection "Outils et modèles mathématiques," Tome 2. Librairie Vuibert, 341 pp.

Joss, J., and A. Waldvogel, 1990: Precipitation measurement and hydrology. *Radar in Meteorology: Battan Memorial and 40th Anniversary Radar Meteor. Conf.*, D. Atlas Ed., Amer. Meteor. Soc., 577–606.

Marzoug, M., and P. Amayenc, 1991: Improved range profiling algorithm of rainfall rate from a spaceborne radar with a path-integrated constraint. *IEEE Trans. Geosci. Remote Sens.*, (Special Issue IGARSS'90), **GE-29,** 584–592.

——, and ——, 1994: A class of single- and dual-frequency algorithms for rain-rate profiling from a spaceborne radar. Part 1: Principle and tests from numerical simulations. *J. Atmos. Oceanic Technol.*, **11,** 1480–1506.

Meneghini, R., and T. Kozu, 1990: *Spaceborne Weather Radar.* Artech House, 199 pp.

——, J. Eckerman, and D. Atlas, 1983: Determination of rainrate from a spaceborne radar using measurements of total attenuation. *IEEE Trans. Geosci. Remote Sens.*, **GE-21,** 34–43.

Probert-Jones, J. R., 1962: The radar equation in meteorology. *Quart. J. Roy. Meteor. Soc.*, **88,** 485–495.

Roux, C., T. Lebel, C. Depraetere, and H. Andrieu, 1989: Simulation à l'aide d'un modèle numérique de terrain des échos de sol détectés par un radar météorologique. *Hydrol. Cont.*, **4,** 139–149.

Skolnik, M. I., 1990: *Radar Handbook.* 2d ed. McGraw-Hill, 1037 pp.